Master's Thesis

Detection feasibility of ultra-intense magnetic field generated in non-central Pb-Pb collisions with dimuon measurement at ALICE

Hiroshima University
Graduate School of Advanced Science and Engineering
Quark Physics Laboratory
M206652

Kento Kimura

Supervisor: Prof. Kenta Shigaki
Chief Examiner: Prof. Kenta Shigaki
Vice Examiner: Prof. Masahiro Kato
Vice Examiner: Associate Prof. Takashi Umeda

January 31, 2022

Abstract

Heavy ions pass each other at almost the speed of light, generating an ultra-intense magnetic field in high energy Heavy ion collisions. The maximum intensity generated in the LHC energy at CERN can reach 10^{14} T $\sim 10^{15}$ T. Nonlinear QED effects, chiral magnetic, and so on have been discussed. But, this magnetic field has not yet been detected experimentally. The purpose of this study is to evaluate the detection feasibility of a ultra-intense magnetic field with ALICE.

We propose to measure the virtual photon polarization, which decays anisotropically into lepton pairs due to an ultra-intense magnetic field as a method to detect an ultra-intense magnetic field. The detection feasibility was estimated based on QED calculations and simulations, and the results show that direct detection of ultra-intense magnetic fields is expected at Run 3 (2022-). We plan to measure the virtual photon polarization by dimuon measurement with transverse momentum (p_{T})>4 GeV/c at Run 3. Since a ultra-intense magnetic field can exist in the initial stage of nuclear collisions and virtual photons generated in the initial stage can be affected by a ultra-intense magnetic field. Prompt photons are one of the direct photon and dominates against the direct photon for p_{T}>4 GeV/c. The ALICE has muon detectors with high capability identified muon. The signal background ratio of muons is higher than that of electrons. The Forward Muon Tracker (MFT), which will be newly installed at Run 3, will improve the track determination accuracy and is expected to have a higher signal to background ratio. Because this is the first attempt of virtual photon polarization measurement with dimuons, it is essential to discuss the feasibility of the measurement. In this study, the significance of virtual photon polarization is evaluated only for the statistics with large contribution, without considering the detector effect.

We estimated the expected significance and evaluated the feasibility of virtual photon polarization measurement. The following (i)-(iii) are important inputs for estimating the significance. (i) the virtual photon polarization, which can be expected by a one-loop QED calculation with the effect of the ultra-intense magnetic field, (ii) the number of dimuons decaying from prompt virtual photons, which is the signal (N_{S}), and (iii) the number of combinatorial unlike-sign dimuons, which is the principal component of the signal background (N_{B}).

Virtual photon polarization could numerically be calculated by vacuum polarization tensor written down to an infinite sum of Landau levels. Numerical calculations were carried out up to the evaluation of the systematic uncertainty by extrapolation to the infinite sum of Landau levels. For virtual photons with p_{T}> 4GeV/c, virtual photon polarization of 0.12±0.03 was found to be expected. By scaling the simulation of proton-proton collisions to Pb-Pb collisions, we estimated the number of dimuons from the initial collision virtual photon(N_{S}). Number of combinatorial unlike-sign dimuons (N_{B}) were estimated by the simulation of Pb-Pb collisions.

We found that the statistics at Run 2 can be expected to have a significance of 1.4σ for p_{T}>4 GeV/c. The significance is expected to increase to 4.3σ at Run 3. The signal background ratio is expected to be improved by the installation of the MFT. There is a good possibility that a significant signal of virtual photon polarization can be detected.

Contents

List of Figures

List of Tables

1 Introduction

1.1 Physics in strong magnetic fields

1.1.1 Non-linear quantum electrodynamics

It is found that perturbation expansions work well because the coupling constant in Quantum Electrodynamics (QED) is small. As a result, various physical quantities can be calculated with very high accuracy, and experiments and theories have been compared. But, it has been pointed out from a paper published in 1936 by W. Heisenberg and H. Euler that the phenomenon of QED in ultra-intense magnetic fields[14] is different from that in vacuum.

In particular, in ultra-intense magnetic fields beyond the critical magnetic field $B_c = m_e^2/|e|$, the contribution up to $(eB/m^2)^n$ to the fermion propagator becomes non-negligible, as shown in Fig.1, and the perturbation calculation will fail. The vacuum becomes unstable due to the pair creation of real particles in the critical field when the contribution up to infinite order is worked. This phenomenon is called nonlinear QED because it works non-perturbatively and non-linearly .

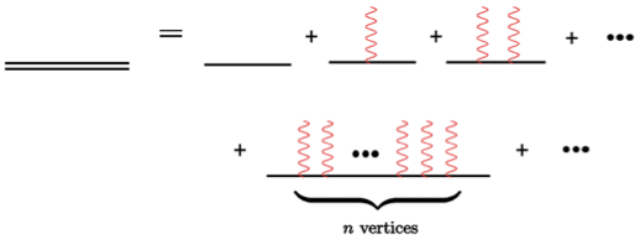

Figure 1: Fermion propagator in unlta-intense magentic field [1]

Vacuum birefringence

The vacuum birefringence of photons is a typical phenomenon of nonlinear QED effects that is possible in ultra-intense magnetic fields. The phenomenon can be obtained by evaluating the one-loop vacuum polarization diagram of a fermion-antifermion pair in an external magnetic field, as shown in the upper part of Fig.2. The presence of an ultra-intense magnetic field gives a specific direction to the system, so that the refractive index of light depends on the direction of the magnetic field. In addition, when the photon energy exceeds a threshold, a complex component is had in the vacuum polarization tensor, allowing lepton pair decay from real photons, which was not possible in vacuum. There are observations or experiments for phenomena due to vacuum birefringence such as X-ray polarization of neutron star[15] and OVAL experiment[16].

Photon splitting

The lower panel in Fig.2 shows a diagram of a single photon splitting into two photons. In a vacuum, Furry's theorem prohibits processes with an odd number of external lines, but in an ultra-intense magnetic field, an even number of external lines contribute. Therefore,

photon splitting and connecting can occur. In high-energy heavy ion collisions, photon splitting can occur, which may the photon energy softer distribution.

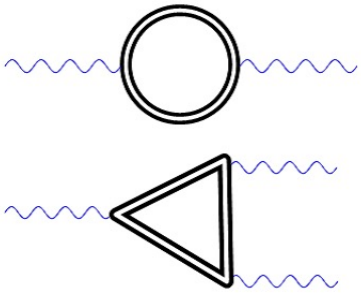

Figure 2: upper:diagram of vacuum birefringence, lower:diagram of photon splitting[2]

1.1.2 Others physics in strong magnetic fields

Chiral magnetic effect[17]

This is not a nonlinear QED phenomenon, but it is an interesting phenomenon that shows the relationship between QED and QCD. Fig.3 shows an illustration of the chiral magnetic effect. The red arrows mean the direction of momentum. The blue arrows mean the spin of the quarks. There are as many left-handed as for right-handed quarks in the initial stage. An ultra-intense magnetic field aligns the direction of the momentum and spin of quarks. A current flows because the right-handed up quarks will move upwards and the right-handed down quarks will move downwards.

The STAR experiment at RHIC aims to observe fluctuations in the charge asymmetry induced by the current [18].

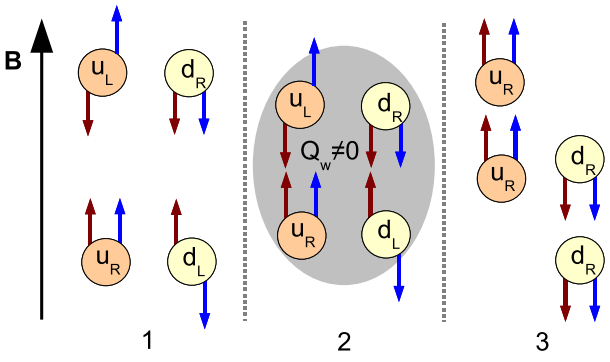

Figure 3: Illustration of the Chiral Magnetic Effect in ultra-intense magnetic field.[3]

Synchrotron radiation of Quark

Quarks are confined by the strong interaction of gluons as medium particles. In the initial universe, quarks were to be in a state where they are free from confinement. This

state is called Quark-Gluon Plasma (QGP). When an ultra-intense magnetic field exists in the QGP, where there are a lot of freed quarks and gluons, the quarks with charges wrap around the magnetic field and emit gluons, just as electrons wrap around magnetic fields and emit photons in synchrotron radiation. As quarks and antiquarks radiate gluons, they lose energy. Since the main cause of energy loss in high energy heavy ion collisions is the strong interaction during the passage through the QGP, the energy loss due to the synchrotron radiation of quarks can be a new cause of energy loss.

1.2 High energy heavy ion collisions

The purpose of high energy heavy ion collisions is to understand the origin of mass by partial restoration of chiral symmetry and the space-time evolution of the universe after the Big Bang by studying the properties of QGP produced by collisions of heavy ions such as Pb and Au accelerated to the relativistic regime. Fig.4 shows the space-time evolution in high energy heavy ion collisions. The states are mainly divided into "Parton scattering", "thermal equilibrium, QGP", "hadronization", and "final state". Nuclei accelerated at high energy collide in a pancake-like state due to Lorentz contraction. At about 1 fm/c after the collision, the temperature of the system exceeds the phase transition temperature (about 150 MeV) due to the scattering of partons in the nuclei. After that, a local thermal equilibrium state is reached and QGP is produced. As the temperature of the system decreases with time, the quarks are trapped again and hadrons are produced. In addition, the unstable hadrons decay to a stable state. At present, high energy heavy ion collisions are being conducted at RHIC, the Relativistic Heavy Ion Collider at Brookhaven National Laboratory in New York, USA, and at LHC, the Large Hadron Collider at CERN in the suburbs of Geneva, Switzerland. Future experiments are expected to further elucidate our understanding of QGP properties, the experimental verification of quantum chromodynamics based on this understanding, and the properties of matter in the early universe and at high temperature extremes.

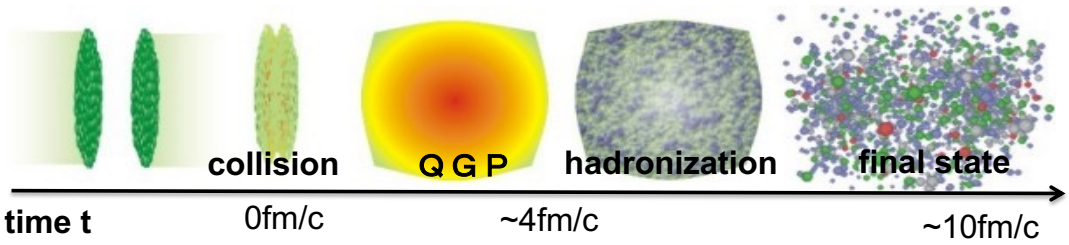

Figure 4: Time-space development of heavy ion collision[4]

1.2.1 Direct Photons in heavy ion collisions

Photons in high energy heavy ion collisions are produced at each stage from the initial stage to the final state, as shown in Fig.4. The photons generated can be divided into hadronic decay photons, which are generated by decaying hadrons, and direct photons, which are generated by other processes. Hadronic decay photons are generated on a time scale of about 10^7 fm/c after the collision, while direct photons are generated on a time scale of

about 10 fm/c. In addition, since photons don't interact with strong interaction, they can pass through the QGP with the information they had at the time of generation. Therefore, the direct photon is an effective probe to study the early stage of collision and the QGP.

Direct photons can be divided into the following three categories according to their generation process

1. Perturbative QCD(pQCD) photons from hard scattering by quark and gluon
2. Thermal photons generated from QGP
3. Hadron gas thermal photons generated in hadron gas

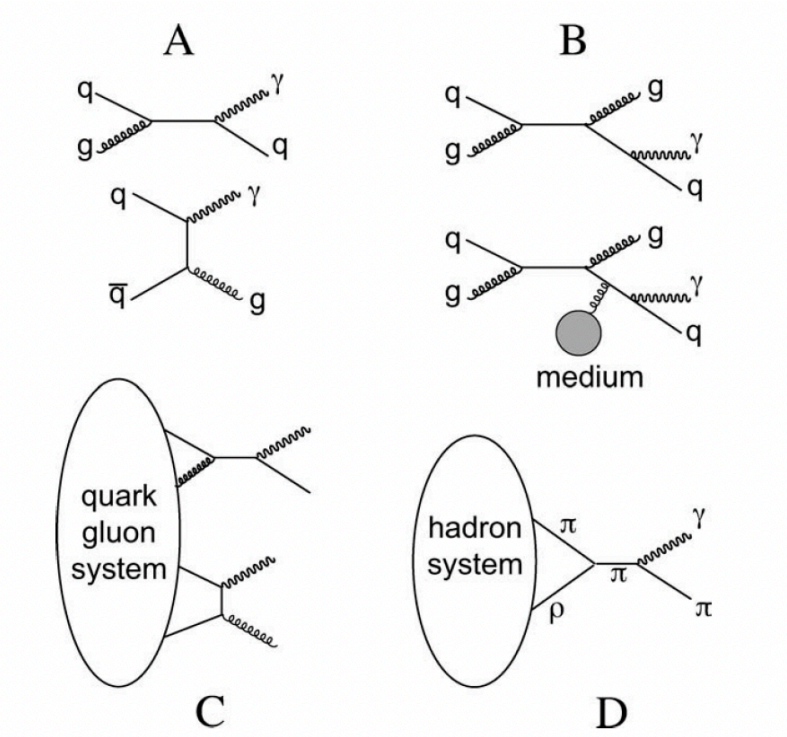

Figure 5: Mechanism of direct photon production in high energy heavy ion collisions[5]

Fig.5 shows the process of direct photon production: A is Compton scattering of quarks and gluons (q+g $\rightarrow$ q+γ) and annihilation of quarks and antiquarks (q+$\bar{q}$ $\rightarrow$ g+γ). B is photon generation by fragmentation. These generation ratios can be calculated by pQCD. C is the thermal photon from QGP. Generation process of pQCD photons and thermal photons from QGP is same. In the case of pQCD photons, the partons in the nucleon are scattered by each other while in the case of thermal photons from QGP, the thermal partons are scattered. D is from hadron gas.

Fig.6 shows the p_{T} distribution of each direct photon process at the ALICE. According to theoretical calculations, thermal photons dominate in the region of 1 GeV/c<p_{T}<4 GeV/c. On the other hand, pQCD photons are dominant in the 4 GeV/c<p_{T} region.

Since the ultra-intense magnetic field is generated at the initial stage of the collision, the simultaneously existing pQCD photons are effective for the virtual photon polarization

measurement. Therefore, it can be seen that it is sufficient to measure dimuons from virtual photons with 4 GeV/c<p_{T} in this study.

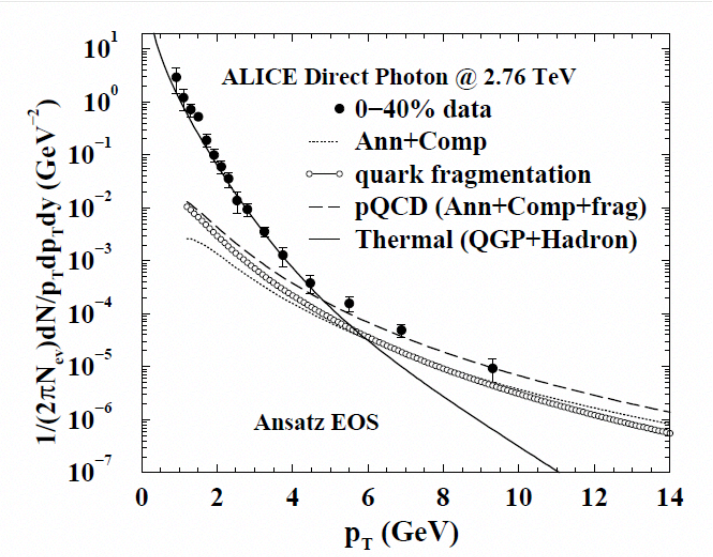

Figure 6: Data and estimation of direct photon in Pb-Pb at $\sqrt{s_{\mathrm{NN}}}$=2.76 TeV[6]

1.3 Ultra-intense magnetic field generated in non-central heavy ion collisions

1.3.1 Generation of ultra-intense magnetic field

In rest system of charged particles, a spherically symmetric Coulomb electric field is distributed, but when the charged particles move at almost the speed of light, the electric field increases in intensity in the direction of motion due to Lorentz contraction. In addition, since the charged particles are in motion, the electric field changes with time. Therefore, a magnetic field of the same intensity is generated. The magnetic field strength generated by a particle with charge Ze can be calculated with Lienard-Wiechert potential, which is derived from Maxwell's equations with relativistic effects, and is written as Eq.1. Here, we assume time t, position of the charged particle $\boldsymbol{r'}$, velocity $\boldsymbol{v}$, and arbitrary position $\boldsymbol{r}$.

$$\boldsymbol{B}(\boldsymbol{r},t) = \frac{Ze\mu_0}{4\pi}\frac{\boldsymbol{v}\times\boldsymbol{R}}{R^3}\frac{(1-v^2/c^2)}{[1-(v/c)^2\sin^2\phi_{Rv}]^{3/2}} \tag{1}$$

Z : atomic number

e : elementary charge

$\boldsymbol{R}$: $\boldsymbol{r}-\boldsymbol{r'}$

$\boldsymbol{r}$: arbitrary position

$\boldsymbol{r'}$: position of charged particle

μ_0 : vacuum permeability

ϕ_{Rv} : angle between $\boldsymbol{R}$ and $\boldsymbol{r}$

Fig.7 shows the generation of an ultra-intense magnetic field in a high energy heavy ion collision. In a high energy heavy ion collision, heavy ions pass each other at nearly the

speed of light. The generated high intensity magnetic field is the sum of the magnetic fields of the spectators, which are not involved in the reaction, and the participants, which are involved in the reaction. The spectators is mainly contributed to the maximum intensity of the magnetic field. In the case of central collisions, the magnetic fields cancel each other out. In the case of non-central collisions, the magnetic field is generated perpendicular to the reaction plane.

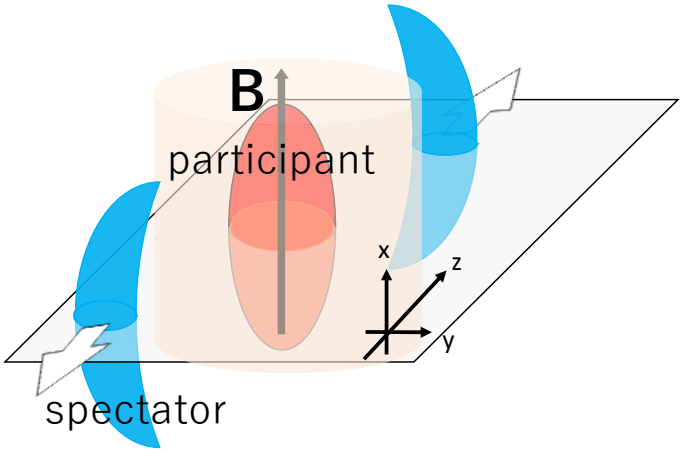

Figure 7: Illustration of non-central heavy ion collision

1.3.2 Intensity and lifetime

The magnetic field intensity was calculated with the Glauber model by Monte Carlo simulation. The Glauber model is a geometric model of high energy heavy ion collisions. Heavy ion collisions are considered to be a superposition of nucleon-nucleon collisions, and nucleons are assumed to move in a straight line and not to bend their orbits after collisions. Secondary particle production and excitation are not taken into account.[19]

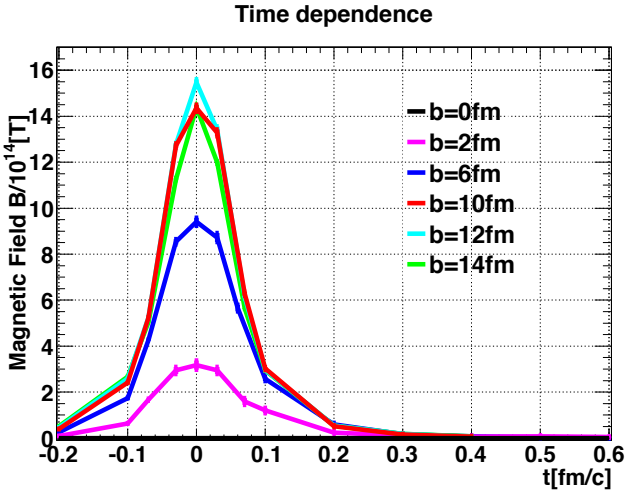

Figure 8: Time dependence and impact parameter dependence of magnetic field generated in non-central Pb-Pb collisions at $\sqrt{s_{\mathrm{NN}}} = 2.76\mathrm{TeV}$[7]

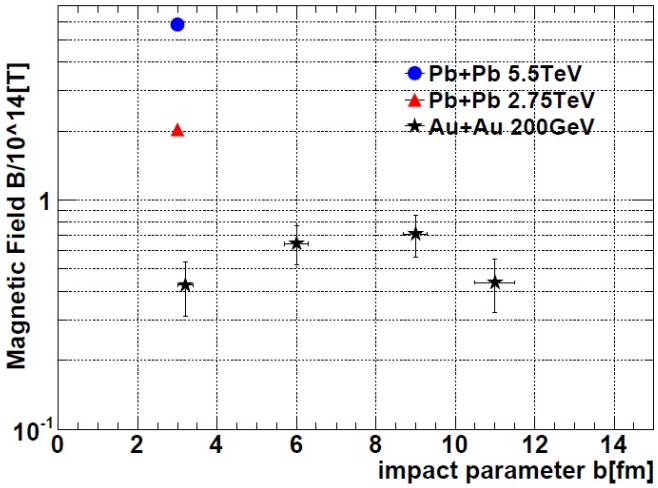

Figure 9: Strength of magnetic field generated by paticipant[7]

As shown in Fig.7, the magnetic field generated in high energy heavy ion collisions is the magnetic field generated by spectators and participants, with the main contribution of spectators. Fig.8 shows time dependence and impact parameter dependence of the magnetic field in high energy heavy ion collisions. In the case of central collisions in all energy regions, a relatively weak magnetic field is produced. As the impact parameter increases, the magnetic field produced becomes stronger, reaching a maximum at a impact parameter of $b = 10 \sim 14$ fm. It can also be seen that the magnetic field becomes stronger in proportion to the collision energy, and the maximum field reaches 10^{15} T in the energy region of the LHC. The maximum field is maintained on a time scale of 0.1 fm/c because spectator flies away at almost speed of light. Fig.9 shows the magnetic field strength generated by the scattering of participants. The magnetic field due to the rotation of the QGP is not taken into account here.

STAR experiment at RHIC measures Λ polarization to detect the magnetic field that is believed to be produced by the angular momentum of QGP in non-central collisions[20].

	Intensity[T]
Neodymium magnet	0.5
Maximum intensity of controlled magnetic field	1200
Critical magnetic field of electrons	4×10^9
Surface magnetic field of a magnetar	10^{11}
Non-central HIC (LHC)	10^{15}

Table 1: Intensity of various magnetic fields

1.4 Virtual photon polarization measurement

In this study, we focused on virtual photon polarization, which is one of the QED nonlinear effects. Because the refractive index of light depends on the direction of the magnetic field due to an ultra-intense magnetic field, the strength of the decay of virtual photons into fermion and anrifermion pairs depends on the direction of the magnetic field. Virtual photons decay anisotropically into fermion and antidermionn pairs due to an ultra-intense

magnetic field. We define this anisotropy as virtual photon polarization. Therefore, the virtual photon polarization can be an evidence of an ultra-intense magnetic field. We defined the virtual photon polarization in virtual photons with only momentum perpendicular to the magnetic field as follows as shown Fig.10

$$P_{\text{meas}} = \frac{N_{\perp} - N_{\parallel}}{N_{\perp} + N_{\parallel}} \tag{2}$$

where P_{meas} is measured Polarization, $N_{\perp}$ is the number of dimuons perpendicular to magnetic field and $N_{\parallel}$ is the number of dimuons parallel to magnetic field.

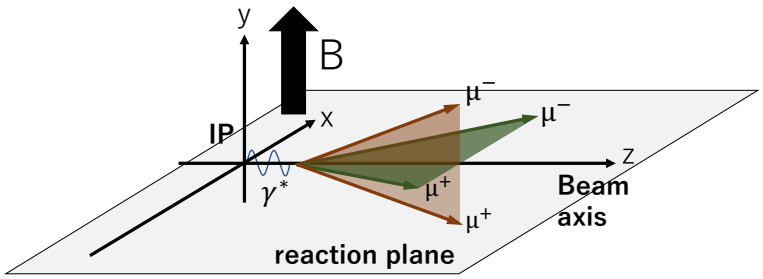

Figure 10: Illustration of virtual photon polarization

1.5 Production rate of dimuons from virtual photons

The dimuon production rate with the effect of the ultra-intense magnetic field can be written as

$$R_{\mu^+\mu^-} = \frac{\alpha^2}{2\pi^4} \mathrm{L}^{\mu\nu}(p_1, p_2) \mathrm{D}_{\mu\alpha}(q.eB) \mathrm{D}^*_{\nu\beta}(q.eB) \frac{\mathrm{ImG}^{\alpha\beta}_R(q, T, eB)}{\mathrm{e}^{q^0/T} - 1} \tag{3}$$

where,

$$\mathrm{L}^{\mu\nu} = p_1^{\mu} p_2^{\nu} + p_1^{\nu} p_2^{\mu} - (p_{12} + m^2) g^{\mu\nu} \tag{4}$$

$$\frac{\mathrm{ImG}^{\alpha\beta}_R(q, T, eB)}{e^{q^0/T} - 1} = (-g^{\alpha\beta} q^2 + q^{\alpha} q^{\beta}) \mathrm{C} \tag{5}$$

$$\mathrm{D}_{\mu\nu}(q, eB) = -\frac{i}{q^2} [g^{\mu\nu} - \frac{1}{q^2} \Pi_{\mu\nu}(q, eB)]^{-1} \tag{6}$$

where p_1 and p_2 are the four-momenta of the μ and anti-μ particles, and $q = p_1 + p_2$ is the four-momentum of the virtual photon.

$L^{\mu\nu}$ is the lepton tensor representing the kinematics of the dimuons after decay.

$\mathrm{G}^{\alpha\beta}_{\mathrm{R}}$ is the Green's function that is the source of virtual photons in thermal and ultra-intense magnetic fields. Describing this source part in high energy heavy ion collisions requires difficult calculations. The source is assumed to be unpolarized and replaced by a conserved current expressed by Eq.5. From the definition of virtual photon polarization, we assume that the source part is canceled out, and replacing it in this way does not affect the result.

$D_{\mu\nu}(q, eB)$ is the propagation function of a virtual photon in an ultra-intense magnetic field. The $\Pi^{\mu\nu}(q, eB)$ is the vacuum polarization tensor with the effect of an ultra-intense magnetic field. Since it is expressed as a complex double integral, it was difficult to calculate analytically. However, numerical calculations have been made possible by [1][21]. In this study, we calculate the probability that a virtual photon with momentum only perpendicular to the magnetic field decays perpendicular to the field $R_\perp$ and parallel to the field $R_\parallel$, and obtain the virtual photon polarization. Since the muon detector at the ALICE is perpendicular to the magnetic field, the calculation is effective enough to estimate the virtual photon polarization.

1.5.1 Vacuum polarization tensor in ultra-intense magnetic field

The vacuum polarization tensor with the effect of an external ultra-intense magnetic field in it, $\Pi^{\mu\nu}$, is expressed as follows[22].

$$\Pi^{\mu\nu}(k) = (P^{\mu\nu} - P_\parallel^{\mu\nu} - P_\perp^{\mu\nu})N_0(k) + P_\parallel^{\mu\nu}N_1(k) + P_\perp^{\mu\nu}N_2(k) \tag{7}$$

where,

$$P^{\mu\nu} = k^2\eta^{\mu\nu} - k^\mu k^\nu,\ \ P_\parallel^{\mu\nu} = k_\parallel^2\eta^{\mu\nu} - k_\parallel^\mu k_\parallel^\nu,\ \ P_\perp^{\mu\nu} = k_\perp^2\eta^{\mu\nu} - k_\perp^\mu k_\perp^\nu \tag{8}$$

The k^μ represents the four-momentum of the virtual photon. The direction of the magnetic field is the z-axis direction, and k^μ and the metric tensor $\eta^{\mu\nu}$ are defined in the direction with respect to the magnetic field as follows.

$$k_\parallel^\mu = (k^0, 0, 0, k^3) = (\omega, 0, 0, k_z),\ \ k_\perp^\mu = (0, k^1, k^2, 0) = (0.k_x, k_y, 0) \tag{9}$$

$$g_\parallel^{\mu\nu} = \mathrm{diag}(1, 0, 0, -1),\ \ g_\perp^{\mu\nu} = \mathrm{diag}(0, -1, -1, 0) \tag{10}$$

$$k_\parallel^2 = \omega^2 - k_z^2 \tag{11}$$

$$k_\perp^2 = -(k^1)^2 - (k^2)^2 = -\vec{k}_\perp^2 \tag{12}$$

The form factor N_j (j=0,1,2) in eq.(7) can be expressed as

$$N_j = -\frac{\alpha}{4\pi}\int_{-1}^{1} dv \int_{0-i\epsilon}^{\infty-0\epsilon} [\tilde{N}_j(z, v)e^{-i\psi(z,v)\eta - i\phi(v;r,\mu)} - \frac{1-v^2}{z}e^{-i\frac{z}{\mu}}]dz \tag{13}$$

$$\tilde{N}_0(z, v) = \frac{\cos(vz) - c\cot(z)\sin(vz)}{\sin(z)} \tag{14}$$

$$\tilde{N}_1(z, v) = (1 - v^2)\cot(z) \tag{15}$$

$$\tilde{N}_2(z, v) = 2\frac{\cos(vz) - \cos(z)}{\sin^3(z)} \tag{16}$$

$$\psi(z, v) = \frac{\cos(vz) - \cos(z)}{\sin(z)} \tag{17}$$

$$\phi(v; r, \mu) = \frac{1 - (1 - v^2)r}{\mu} \tag{18}$$

where the dimensionless quantities μ, r, and η are defined as follows

$$\mu = \frac{eB}{m^2},\quad r = \frac{k_\parallel^2}{4m^2},\quad \eta = \frac{2q}{\mu}\quad \text{where,}\quad q = \frac{\vec{k}_\perp^2}{4m^2} \tag{19}$$

Since it is a complicated double integral as in Eq.13, analytical calculations have been difficult. Calculations have been performed only under limited conditions, such as the red and green regions in Fig.11 [23, 24, 25].

In 2012, Hattori and Itakura wrote down the integrand function of the double integral in the form of a double infinite sum of Landau levels originating from fermion and antifermion pais as follows[1]. Thus, the all region of Fig.11 can be verified numerically.

$$\chi_{\mathrm{i}} = \frac{\alpha B_r}{4\pi} e^{-\eta} \sum_{\mathrm{l}=0}^{\infty} \sum_{\mathrm{n}=0}^{\infty} \Omega^{\mathrm{n}}_{\mathrm{l,i}}, \qquad \mathrm{i} = 0, 1, 2 \tag{20}$$

The line in Fig.11 is the threshold at which a photon decays into a fermion and antifermion pair. A photon decays when its longitudinal momentum exceeds the right-hand side of eq.20, which is determined by the Landau level.

$$q_{\parallel}^2 = \left\{ \sqrt{m^2 + 2\mathrm{l}eB} + \sqrt{m^2 + 2(\mathrm{l}+\mathrm{n})eB} \right\}^2 \tag{21}$$

where l and n are Landau levels and $q_{\parallel}^2$ is the longitudinal momentum of the photon.

For the evaluation of the vacuum polarization tensor in the LHC energy region, a tabular expression for the sum of Landau levels that is easy to renormalize was obtained by Ishikawa et al. [21]. The formula for the form factor Eq.13 cannot be calculated numerically because it has already been renormalized. It can be transformed into two separate terms, one for $r \neq 0$ (first term) and one for $r = 0$ (second term). The first term is transformed into a series by the method used by Hattori and Itakura, and the second term is written as Eq.23 because it is analytically connectable.

$$\begin{aligned} \mathrm{N_j} = & - \frac{\alpha}{4\pi} \int_{-1}^{1} dv \int_{0-i\epsilon}^{\infty-0\epsilon} [\tilde{N}_{\mathrm{j}}(z,v) e^{-i\psi(z,v)\eta} (e^{-i\phi(v;r,\mu)} - e^{-i\frac{z}{\mu}})] dz \\ & - \frac{\alpha}{4\pi} \int_{-1}^{1} dv \int_{0-i\epsilon}^{\infty-0\epsilon} [(\tilde{\mathrm{N}}_{\mathrm{j}}(z,v) e^{-i\psi(z,v)\eta} - \frac{1-v^2}{z}) e^{-i\frac{z}{\mu}})] \end{aligned} \tag{22}$$

$$\begin{aligned} \mathrm{N_j} = & - \frac{\alpha}{4\pi} \sum_{n=0}^{\infty} C_{\mathrm{n}} \sum_{\mathrm{l}=0}^{\infty} \Omega^{\mathrm{n}}_{\mathrm{lj}}(r,\eta,\mu) \\ & - \frac{\alpha}{4\pi} \int_{-1}^{1} dv \int_{0-i\epsilon}^{\infty-0\epsilon} [(\tilde{\mathrm{N}}_{\mathrm{j}}(z,v) e^{-i\psi(z,v)\eta} - \frac{1-v^2}{z}) e^{-i\frac{z}{\mu}})] \end{aligned} \tag{23}$$

In this study, the virtual photon polarization is obtained by numerical calculation of the vacuum polarization tensor with Eq.(23).

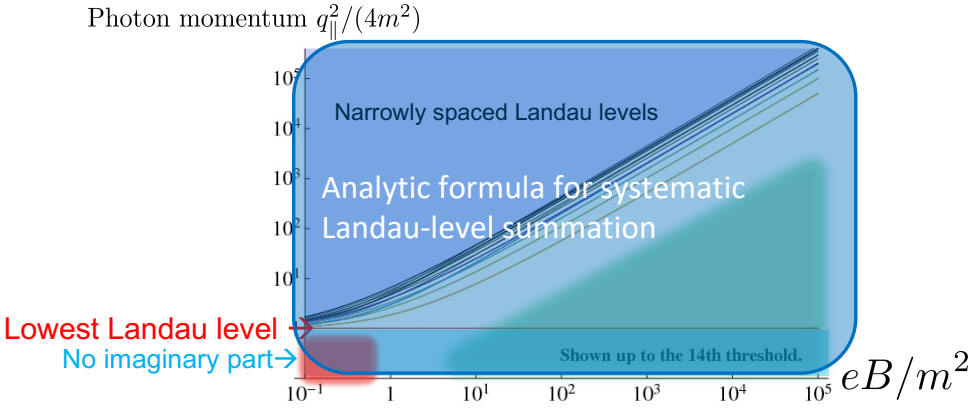

Figure 11: Theoretical interpretation of the vacuum polarization tensor in terms of photon longitudinal momentum and magnetic field strength[8]

1.6 Purpose

We aim to directly detect the ultra-intense magnetic fields in high energy heavy ion non-central collisions. In the past, the detection feasibility of electron-positron pairs as probes has been discussed in the experimental data of Pb-Pb collisions at $\sqrt{s_{\rm NN}}$=2.76 TeV per nucleon at the LHC [19][7], but the detection of the ultra-intense magnetic fields has not yet been achieved. Therefore, we focused on dimuons which don't have π^0 Dalitz decay, which is the main signal background in the electron-positron pair measurement. Furthermore, the ALICE has a muon detector with high capability of identified muons . Therefore, we plan to detect the ultra-intense magnetic fields with dimuon measurement. In our plan to measure vitutla photon polarization with dimuon in the forward region, the virtual photon polarization is estimated by [26].

In this study, we evaluate the systematic error for the theoretical estimation of the virtual photon polarization. Based on the theoretical estimation of the polarization and simulations, we will also evaluate the detection feasibility of ultra-intense magnetic fields during the next operational period of the ALICE.

2 Experimental circumstances

2.1 Large hadron collider (LHC)

The Large Hadron Collider (LHC) is a hadron collider built by CERN in the suburbs of Geneva, Switzerland. Straddling the border between France and Switzerland, the LHC is located at 50 m∼100 m underground and has a circumference of 27 km. At Run 2 (2015-2018), the LHC achieved a center-of-mass collision energy of 13 TeV in pp collisions and 5.02 TeV per nucleon in Pb-Pb collisions. At Run 3 starting in 2022, the LHC plans to reach 14 TeV in pp collisions and 5.5 TeV per nucleon in Pb-Pb collisions.

There are four major experiments at the LHC: ALICE, CMS, ATLAS, and LHCb. Each experiment aims to achieve different physics. For example, the ATLAS and CMS experiments focus on high-energy pp collisions at the LHC and analyze the particles produced by the collisions to discover supersymmetric particles, which may lead to the elucidation of dark matter in the universe, and to explore new physics beyond the Standard Model.

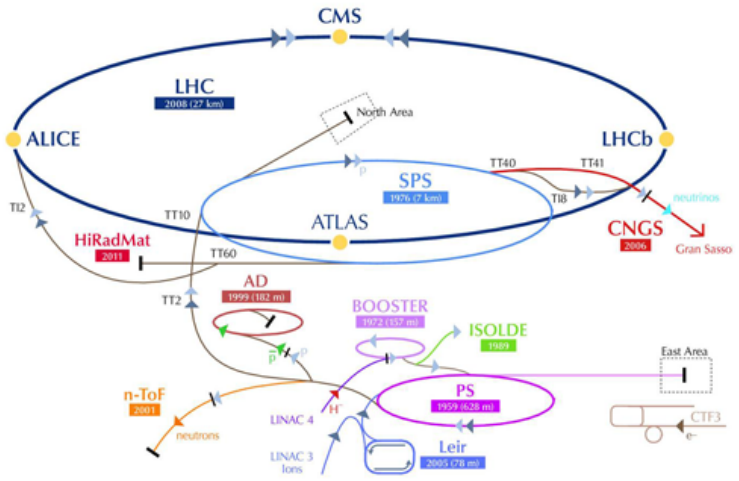

Figure 12: Diagram of LHC[9]

2.2 A Large Ion Collision Experiment (ALICE)

In Pb-Pb collisions at the LHC, the temperature reaches 300 MeV∼600 MeV, which is more than 10^6 times the temperature at the center of the Sun. Since this temperature exceeds the phase transition temperature between the non-confined and material phases of quarks, we believe that it reproduces the state of the universe immediately after the Big Bang, when quarks in nucleons were released from confinement. This provides a clue to how the matter that constitutes the present universe was created during the cooling process from the Big Bang to the expansion of the universe.

The ALICE is the only experiment at the LHC that focuses on heavy ion collisions, which produce thousands of different particles when heavy ions accelerated by the LHC collide with each other. Therefore, detectors are designed to measure many physics such as particle identification, momentum, energy, and so on. In particular, measurement of the soft process probe is a strong point for ALICE. The entire detector is 16 meters high, 16 meters wide, 26 meters long, and weighs 10,000 tons in total. The entire detector is shown in

Fig.13. Members from 40 countries, including France and Italy, and 172 research institutes are participating in this large-scale experiment. From Japan, Hiroshima University, the University of Tokyo, University of Tsukuba, Nagasaki Institute of applied Science, Nara Women's University, and Saga University are ALICE members.

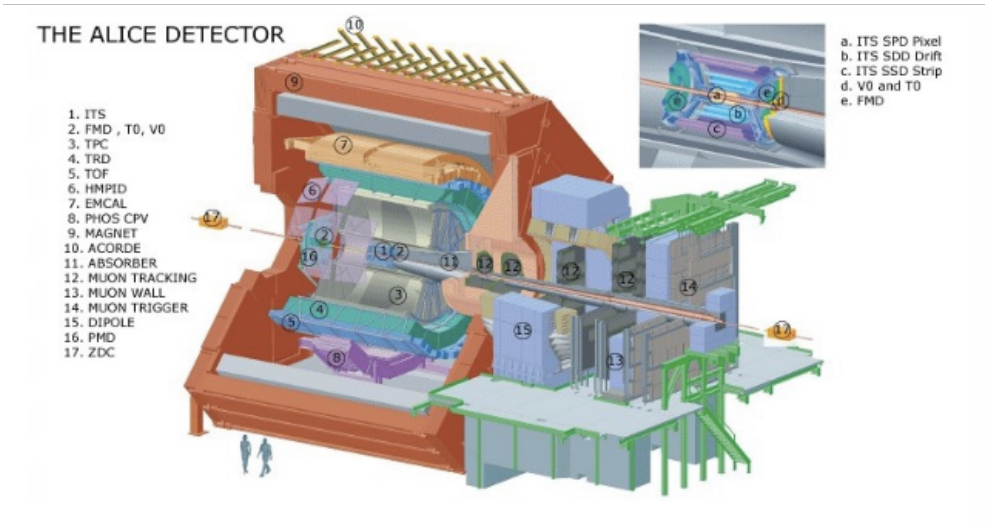

Figure 13: Diagram of ALICE detector[10]

2.2.1 Muon measurement at ALICE

To study the quark-unconfined matter produced by heavy ion collisions, it is necessary to measure the particles that serve as probes. Among the particles generated, leptons are not affected by strong interactions because they don't have a color charge, so they can be measured with the information at the time of production. In addition, compared to electrons, the second-generation leptons, muons, have lower background events and higher permeability, making them easier to identify.

At Run 2, we didn't take data from all collisions, but selected collisions for data acquisition based on triggers. The statistics of all the collisions can be calculated by multiplying the number of events obtained by the trigger by the normalization factor. In this study, the number of minimum bias events obtained by [27] was used as a reference and summarized in Table 2.

2.2.2 Muon spectrometer

In the ALICE, the muon spectrometer shown in Fig.14 is used to measure the trajectory and momentum of a muon. The muon spectrometer covers a pseudo-rapidity region of -4

Periods	N_{MCUL}	F_{norm}	N_{MB}
LHC15o	1.2×10^8	11.88	1.4×10^9
LHC18q	1.1×10^8	13.55	1.5×10^9
LHC18r	1.6×10^8	13.65	2.2×10^9
All	3.9×10^8		5.1×10^9

Table 2: Minimum bias statistics at Run 2

$< \eta <$-2.5. The closest point to the impact point is the absorber, which absorbs particles other than muon at $z =$ -0.9 m to $z =$ -5.03 m. All particles passing through the absorber are considered muons. In addition, five Pad chambers and a Diplemagnet located between $z =$ -5.2 m and $z =$ -14.4 m are used to reconstruct the trajectory and measure the momentum.

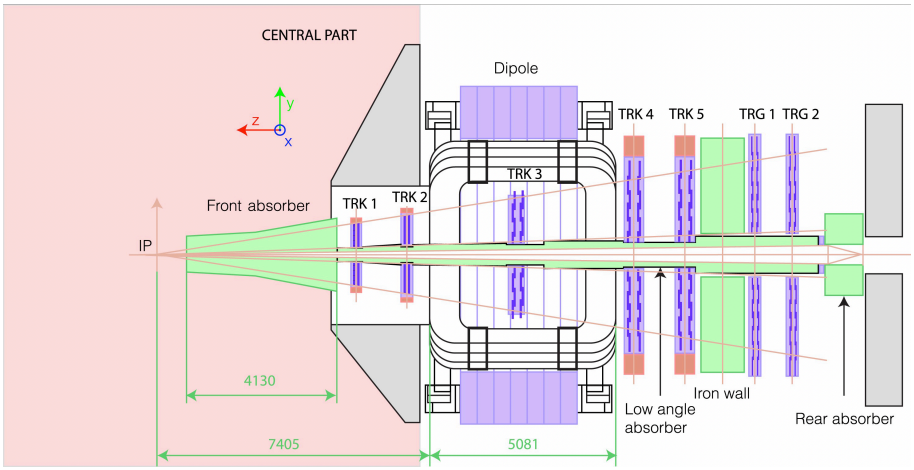

Figure 14: Diagram of muon spectrometer[11]

2.2.3 Muon Forward Tracker (MFT)

The ALICE is a long shutdown starting in 2019 to improve detector capabilities and install new detectors. ALICE at Run 3, which will start in 2022, was installed the Muon Forward Tracker (MFT).[28]

The MFT consists of five disks at z=-460 mm, -493 mm, -531 mm, -687 mm, and -768 mm as shown in Fig.15, covering a range of -3.6$< \eta <$-2.45. Within the absorber of the muon spectrometer. In the absorber of muon spectrometer, it is difficult to reconstruct the precise trajectory due to multiple scattering of muons. The MFT is placed between the interaction point and the absorber, and it is expected to measure the trajectory of the muons before they enter the absorber to reconstruct the trajectory more accurately. This will allow us to improve the resolution of mass of low-mass dimuons and to identify between charm and beauty. It is also expected to be able to identify between muons directly generated at the

collision site and background muons.

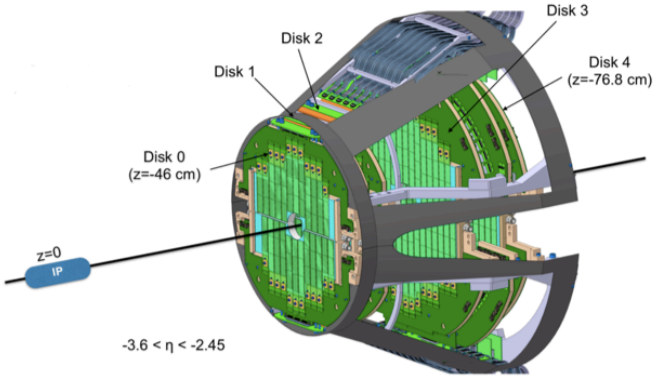

Figure 15: Diagram of MFT[12]

3 Numerical evaluation of virtual photon polarization

In this section, we will discuss the estimation of the virtual photon polarization by numerical calculation, including the effect of the external ultra-intense magnetic field with 10^{15}T. The virtual photon polarization to be measured is defined by 1.4, and the virtual photon polarization to be numerically calculated is defined as follows.

$$P_{\rm cal} = \frac{R_\perp - R_\parallel}{R_\perp + R_\parallel} \tag{24}$$

where $P_{\rm cal}$ is calculated Polarization, $R_\perp$ is the production rate of dimuons perpendicular to a magnetic field, and $R_\parallel$ is the production rate of dimuons parallel to the magnetic field.

3.1 Polarization extrapolation to infinite summation of landau level

The convergence of the form factor in vacuum polarization tensor has been verified by [21], and it was found that the upper limit of l ($\rm l_{max}$) is well converged at 20000. However, the convergence of n was not confirmed. Therefore, we calculated at fixed $\rm l_{max}$=20000 and $\rm n_{max}$=2000, 3000, 4000, 5000, 10000, 20000, respectively. Due to the difficulty in finding a function for $\rm n_{max}$ of the virtual photon polarization, we extrapolated $\rm n_{max}$ to infinity with a polynomial. Here, $\rm n_{max}$ was replaced with $\rm n_{max}^{-1}$, $\rm n_{max}^{-1/2}$, $\rm n_{max}^{-1/3}$, and $\rm n_{max}^{-1/4}$ in order to converge in the direction of the origin of the coordinates when $\rm n_{max}$ was extrapolated to infinity. Originally, it would have been preferable to replace each point with linear function that could fit, but since the function was unknown, we kept it simple. We extrapolated these plots by fitting them with polynomials from the first to the fourth order.

Fig.16-19 shows results calculated at each $\rm n_{max}$ and fitted with polynominals from 1st to 4th order. In Fig.16, it is well-fit from 2nd to 4th by a curve. In Fig.17, it is closer to a straight line and has better properties for extrapolation. In Fig.18 and Fig.19, they were found to have similar properties. Polynomials with the 3rd and 4th order jump at $\rm n_{max}$ infinity when fit.

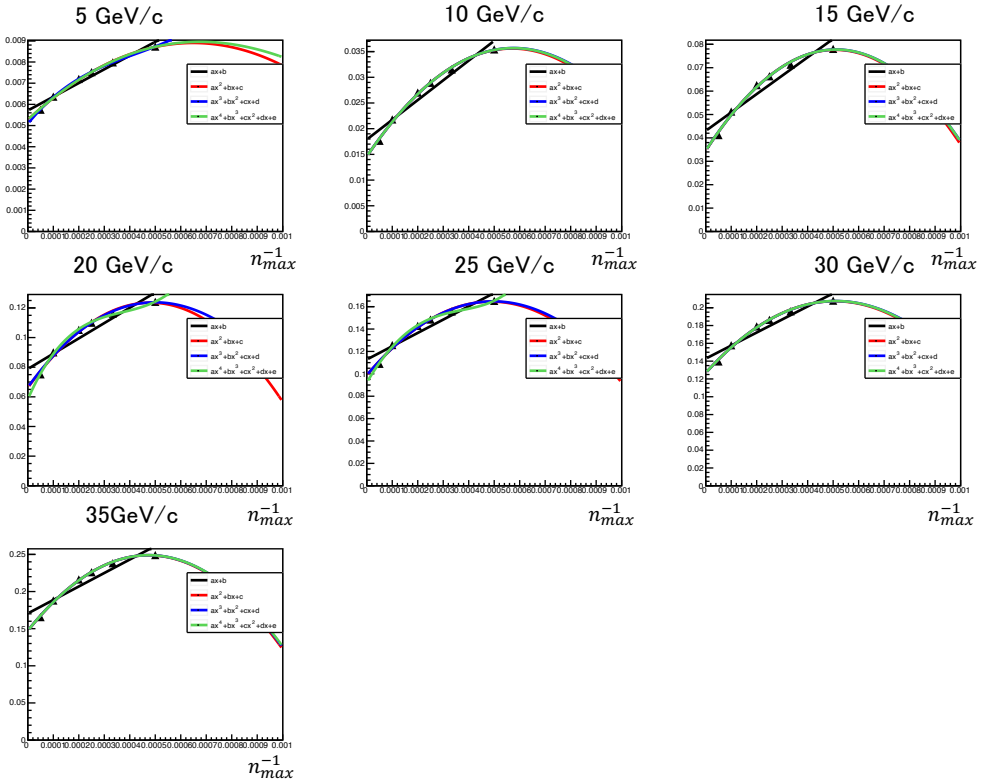

Figure 16: Fitting results with n_{max}^{-1} by four function

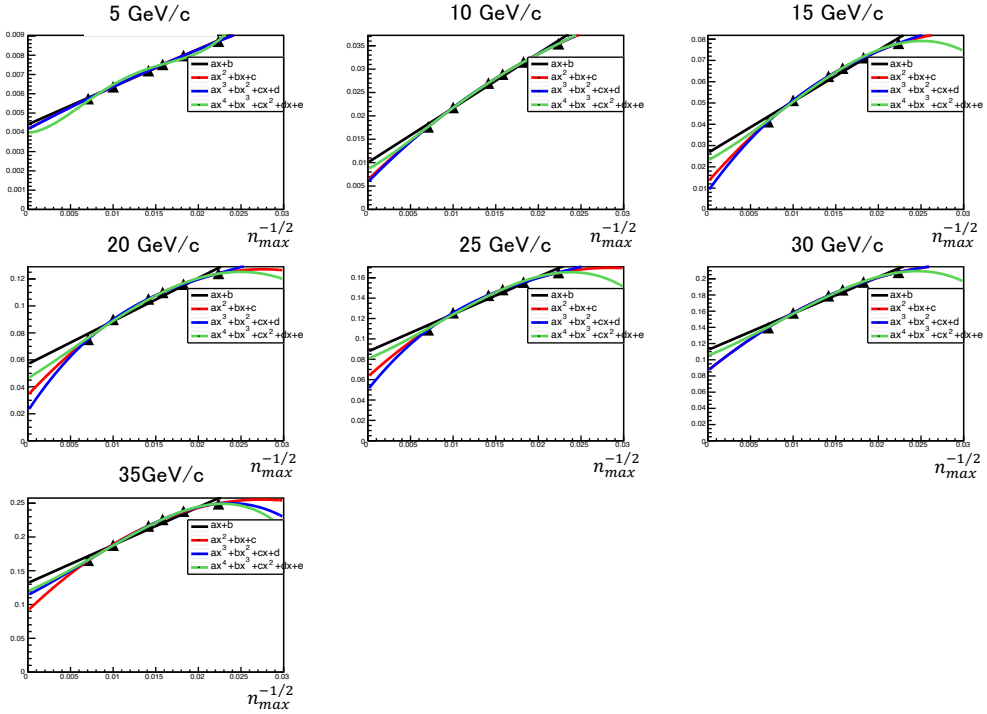

Figure 17: Fitting results with $n_{max}^{-1/2}$ by four function

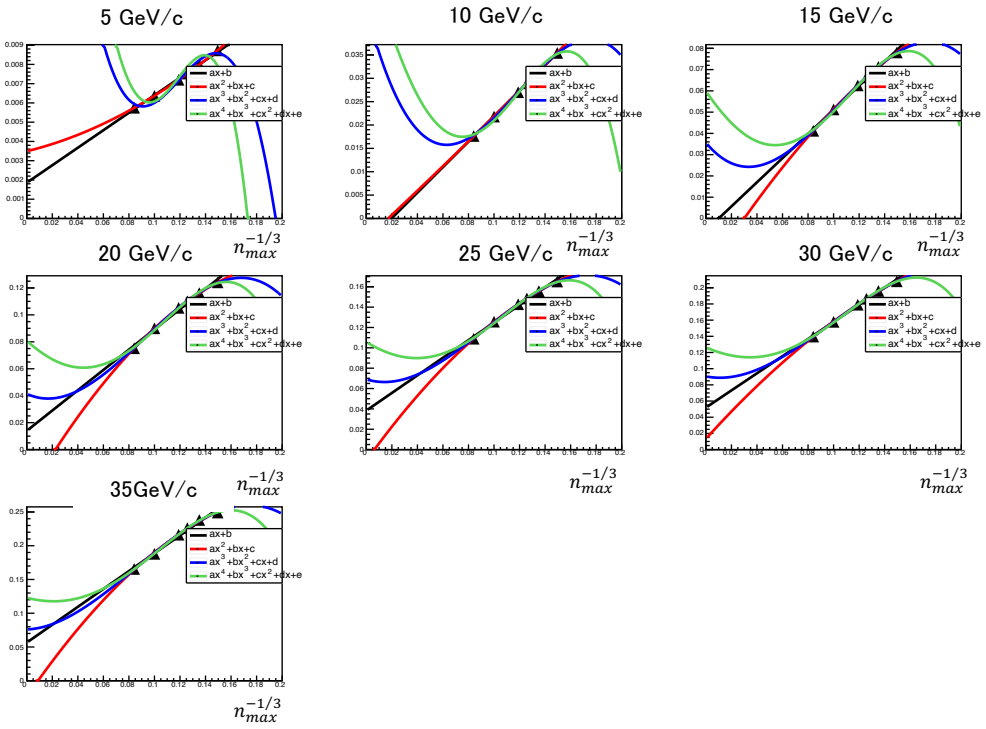

Figure 18: Fitting results with $n_{max}^{-1/3}$ by four function

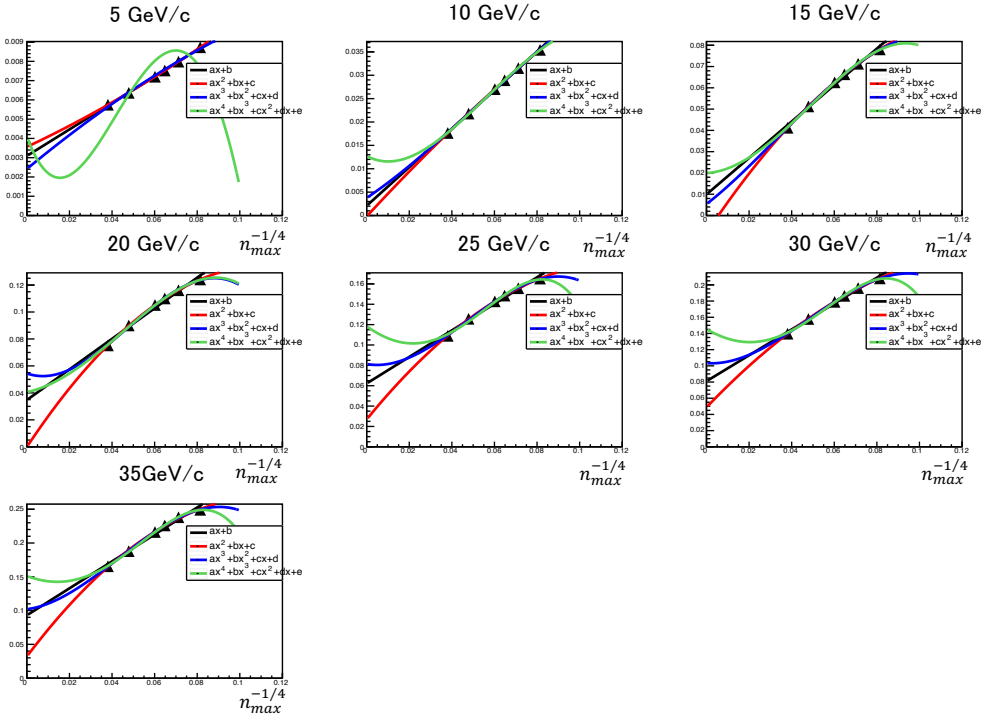

Figure 19: Fitting results with $n_{max}^{-1/4}$ by four function

3.2 Systematic uncertainty

Systematic uncertainty due to extrapolation will be discussed.

We obtained 16 values from extrapolation from 4 polynomials each with 4 different functions. However, Fitting with polynomials with the 3rd and 4th order on two function, $n_{max}^{-1/3}$ and $n_{max}^{-1/4}$, is wrong properties for extrapolation without reason. The Extrapolation with the first and second order on them can be overestimated because of the large uncertainty due to the distance from the origin. Therefore, The systematic uncertainty was calculated from the 8 extrapolation results obtained from these.

In this estimation, we considered the true polarization to be between the largest and smallest of the eight values obtained from the extrapolation. Therefore, the range of uncertainty was set from the maximum to the minimum, and the central value was set as the average of the 8 values.

3.3 Mass dependence

Since the decay from a virtual photon to a dimuon, the mass of the virtual photon must be heavier than about 210 MeV/c^2. Therefore, we calculated the virtual photon mass $M_{\mu\mu}$ at 300 MeV/c^2 $\sim$ 600 MeV/c^2. The results show that the virtual photon polarization is larger as a mass of a virtual photon is lower, as shown in Fig.20. This mass dependence is also consistent with the fact that the photon propagation function has a factor of p^{-1}. As will be discussed in detail in the next section, it was found that the virtual photon polarization in the experiment could be larger because the virtual photon with lower mass has a higher yield.

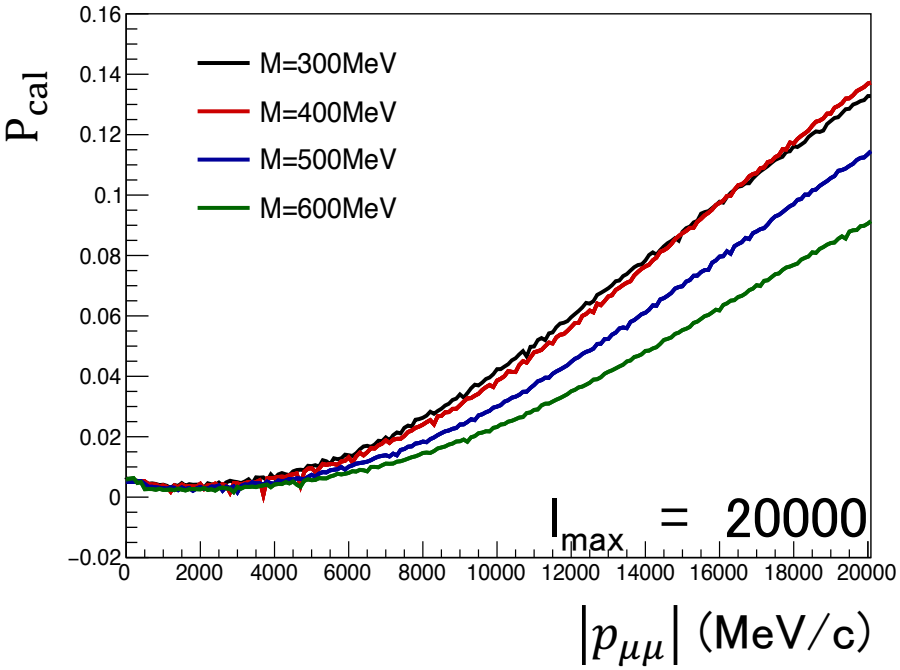

Figure 20: Mass dependence of virtual photon Polarization

3.4 Total momentum dependence

In this section, we show the results for the virtual photon polarization at $M_{\mu\mu}$=300 MeV/c^2, which is the larger contribution of the virtual photon polarization measurement. The virtual photon polarization obtained by the method shown in Sec.3.2 is found to be 0.12±0.03 when the transverse momentum of the virtual photon is about 3.5 GeV/c, as shown in Fig.21. Furthermore, the virtual photon polarization increases with the total momentum of virtual photon. Therefore, higher virtual photon polarization are expected in the measurement region p_{T}>4 GeV/c.

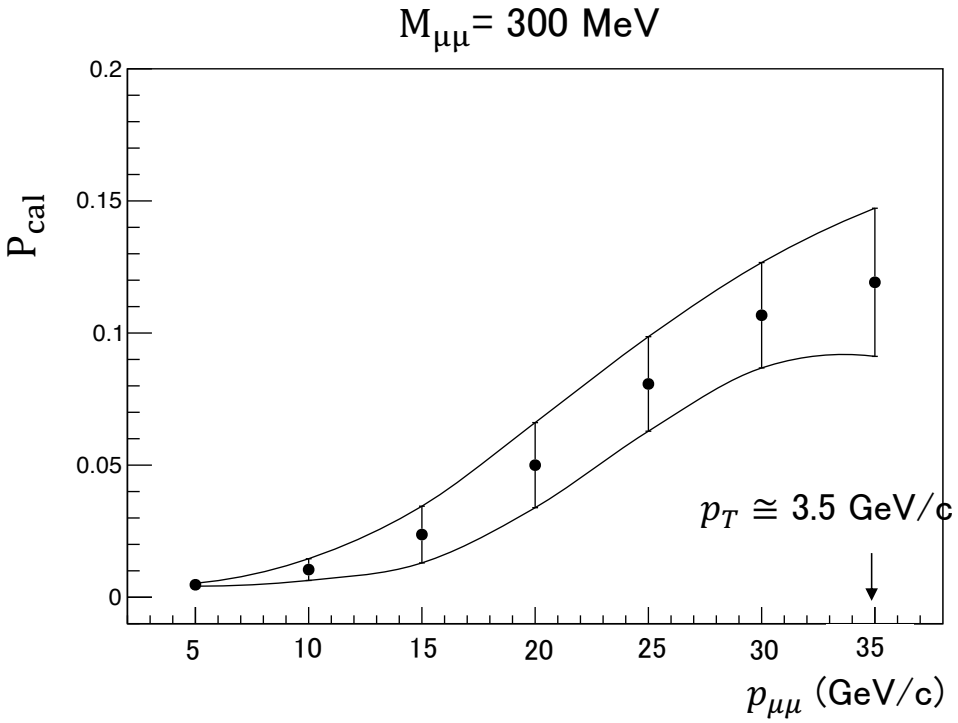

Figure 21: Polarization of virtual photon with 300 MeV/c^2 as a function of total momentum

4 Yield Estimation of signal and Background

In this study, we estimated the yields for each orientation by the method shown in Sec.5. In this section, we will only discuss the estimation of the signal and background yields by Monte Carlo simulation.

4.1 Yield estimation of $\gamma^* \to \mu\mu$ in Pb-Pb

We the yield of $\gamma* \to \mu\mu$ in centrality 40∼60% of Pb-Pb collisions at $\sqrt{s_{\rm NN}}$=5 TeV. Since the prompt virtual photon is generated by hard scattering between partons present in the nucleon during the initial stage, it can be considered as a superposition of pp collisions.

The procedure for estimating the signal yield in Pb-Pb collisions with PYTHIA is as follows

1. pp collisions at $\sqrt{s_{\rm NN}}$=5 TeV are generated as 10^8 events
2. Select direct virtual photons from the following conditions
   (a) The final state must be a muon
   (b) The final state must be a dimuon generated from one parent particle.
   (c) A parent particle of a dimuon must be a photon
   (d) The parent photon must be generated by parton scattering.
   (e) A dimuon must be -4.0 < η < -2.5.
3. Scale to Pb-Pb collisions by the scaling factor in Eq.25

$$S = N_{coll} \times \frac{\text{Stat at Run 2 or 3}}{\text{Minimum bias stat by PYTHIA}} \times \frac{20\%}{100\%} \tag{25}$$

   where, $N_{\rm coll}$ at centrality 40% ∼ 60% is 140[29], Minimum bias statistics by PYTHIA is 10^8 events, stat at Run 2 or 3 is Table 2.
4. Also scale to Pb-Pb collisions in dimuons with $p_{\rm T}$>4 GeV/c

Fig.22 and Fig.23 show the mass and transverse momentum spectrum from pp collisions, respectively. The yield of $\gamma* \to \mu\mu$ scaled to Pb-Pb collisions is summarized in Table 3. For all dimuons at Run 2 statistics, $N_{\rm S} \sim 10^5$ and $p_{\rm T}$ cut was $N_{\rm S} \sim 10^4$.

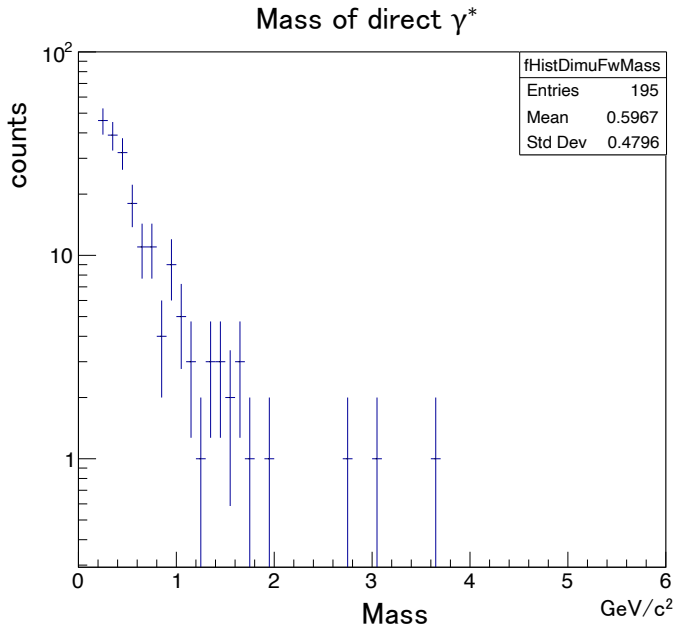

Figure 22: Mass spectrum of virtual photon in pp collisions 10^8 events

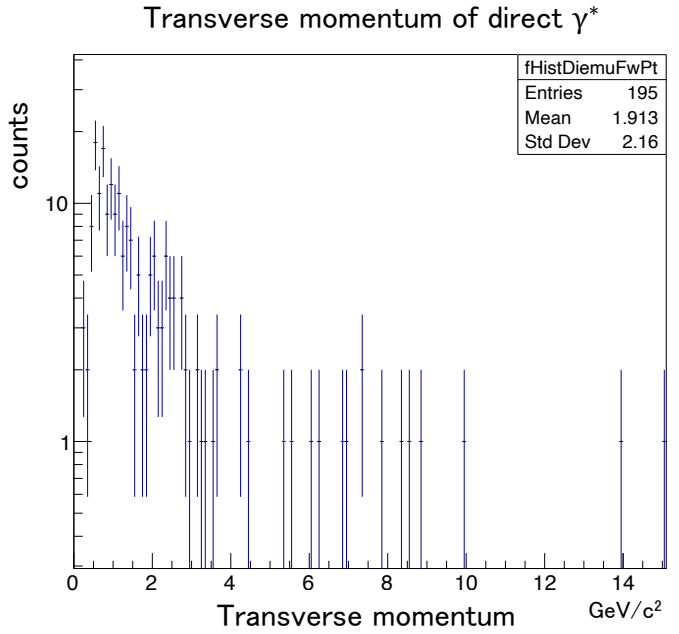

Figure 23: Transverse momentum spectrums of virtual photon in pp collisions 10^8 events

4.2 Estimation of combinatorial background in Pb-Pb

The procedure for estimating the combinatorial background, which is main background in virtual photon polarization measurement, in Pb-Pb collisions with PYTHIA is shown below.

1. Generation of 10^6 events for Pb-Pb collisions at $\sqrt{s_{\mathrm{NN}}}$=5 TeV

2. Selection of events with centrality 40% $\sim$ 60%.

3. Selection muons from the following conditions

   (a) The final state must be a muon

   (b) Muons is -4.0 $< \eta <$ -2.5

   (c) Muons is generated from the interaction point to the edge of the absorber as indicated by the orange arrow in Fig.24.

4. Calculation of mass and transverse momentum for all combinations of unlike-sign dimuons in the same event

5. Scale to a Run 2 or 3 statistics by the scaling factor in Eq.26.

$$S = \frac{\text{stat at Run 2 or 3}}{\text{Minimum bias stat by PYTHIA}} \tag{26}$$

   where, the minimum bias stat by PYTHIA is a 10^6 event and the statistics at Run 2 or 3 is Table 2.

6. Also scale with dimuons for p_{T}>4 GeV/c

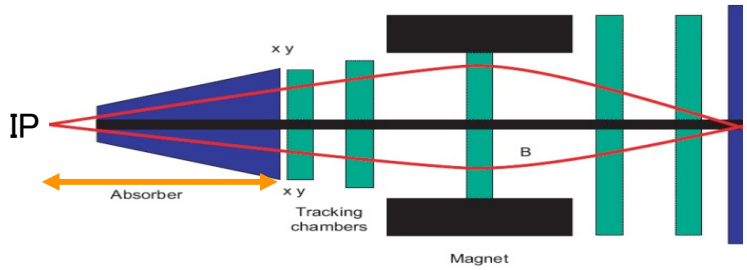

Figure 24: Illustration of indication the region where muon are generated[13]

Fig.25 and Fig.26 show the mass and transverse momentum spectrums of the combinatrial unlike-sign dimuons in Pb-Pb collisions, respectively. In the measurement regime p_{T}>4 GeV/c, the combinatorial background yields are summarized in Table 3 as in the previous subsection. Background for all dimuons in the Run 2 statistics is $N_{\mathrm{B}} \sim 10^{10}$ while background with p_{T} cut is reduced by four order. It is found that the p_{T} cut is a essential effective cut in virtual photon polarization measurement.

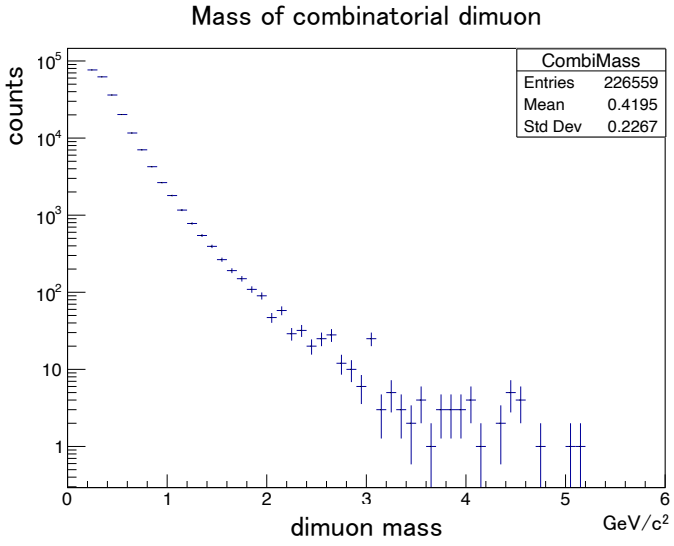

Figure 25: Mass spectrum of combinatorial unlike-sign dimuons in Pb-Pb collisions 10^6 events

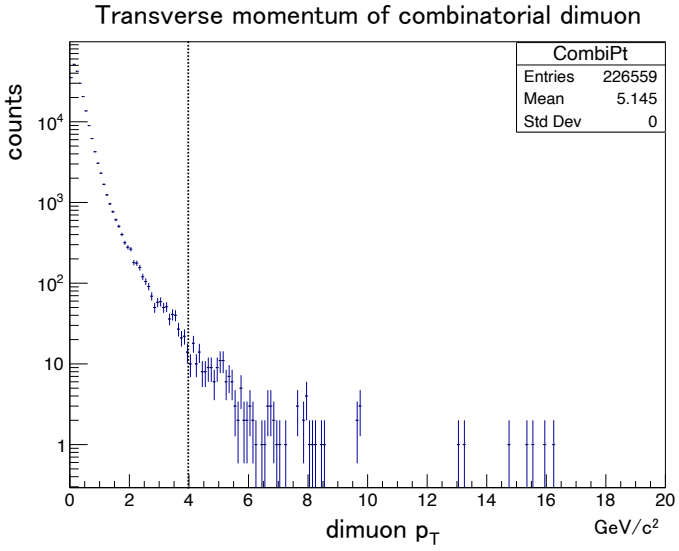

Figure 26: Transverse momentum spectrum of combinatorial unlike-sign dimuons in Pb-Pb collisions 10^6 events

Periods	Cuts	N_s	N_B
Run 2	All dimuons	$\sim 10^5$	$\sim 10^{10}$
	$p_T > 4$GeV/c	$\sim 10^4$	$\sim 10^6$
Run 3	All dimuons	$\sim 10^6$	$\sim 10^{11}$
	$p_T > 4$GeV/c	$\sim 10^5$	$\sim 10^7$

Table 3: Estimated Yield of signal and background

5 Significance estimation of virtual photon polarization

In this section, we discuss the virtual photon polarization estimated by Sec.3 and Sec.4, and the virtual photon polarization expected to be measured in Runs 2 and 3 based on the signal and combinatorial background yields. The virtual photon polarization is defined as the difference between the number of dimuons perpendicular or parallel to the ultra-intense magnetic field. Since the direction of the decay plane of dimuon with respect to the magnetic field follows a binomial distribution, the error of the virtual photon polarization is calculated using the variance. The virtual photon polarization was defined as in Eq.27.

$$P_{\mathrm{meas}} \pm \Delta P_{\mathrm{meas}} = \frac{\langle N_{\perp} \rangle - \langle N_{\parallel} \rangle}{\langle N_{\perp} \rangle + \langle N_{\parallel} \rangle} \pm \frac{2}{\langle N_{\perp} \rangle + \langle N_{\parallel} \rangle} \sqrt{\frac{\langle N_{\perp} \rangle \langle N_{\parallel} \rangle}{\langle N_{\perp} \rangle + \langle N_{\parallel} \rangle}} \tag{27}$$

The expected values of the number of dimuon perpendicular and parallel to the ultra-intense magnetic field can be written by the three estimated values as in Eq.28 and Eq.29.

$$\langle N_{\perp} \rangle = \frac{1}{2} N_{\mathrm{B}} - \frac{1 - P_{\mathrm{cal}}}{2} N_{\mathrm{S}} \tag{28}$$

$$\langle N_{\parallel} \rangle = \frac{1}{2} N_{\mathrm{B}} + \frac{1 - P_{\mathrm{cal}}}{2} N_{\mathrm{S}} \tag{29}$$

Significance, which is important for the detection feasibility of the ultra-intense magnetic field, is defined as Eq.30.

$$\mathrm{Significance} = \frac{P_{\mathrm{meas}}}{\Delta P_{\mathrm{meas}}} \tag{30}$$

Fig.27 is the virtual photon polarization at Runs 2 and 3 obtained with the number of all dimuons. Fig.28 also shows the virtual photon polarization at Runs 2 and 3 for dimuons with p_{T}>4 GeV/c. From these results, it is clear that the significance is improved by applying p_T cut. Furthermore, we found that 1.4σ is expected at Run 2. At Run 3, where the statistics of 10 times muons is expected, the significance is expected to improve by 4.3σ.

	Run 2	Run 3
All dimuons	0.3σ	0.9σ
p_{T}>4 GeV/c	1.4σ	4.3σ

Table 4: Estimated significance for ultra-intense magnetic field detection

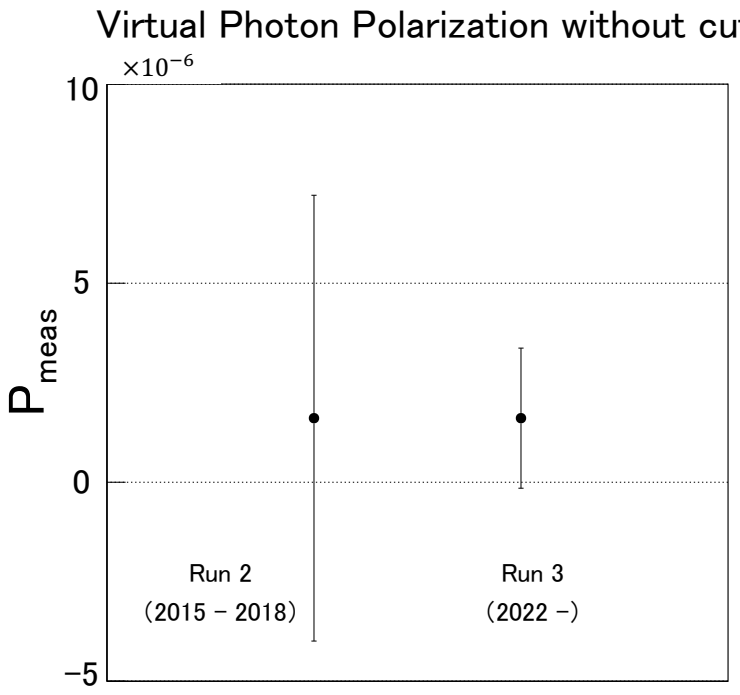

Figure 27: Expected significance of polarization without cut at Runs 2 and 3

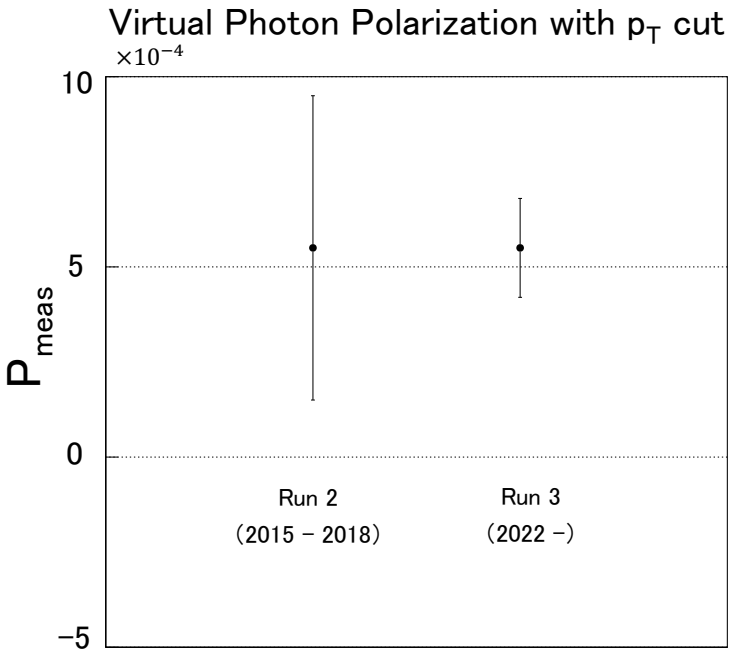

Figure 28: Expected significance of polarization with p_T cut at Runs 2 and 3

This significance was obtained by discussing the statistics only. In actual measurements,

it is necessary to take into account effects such as detector resolution, misidentification and so on. Therefore, the significance obtained in this study may change, but it is expected to be of order 1σ because it takes into account the cut of the transverse momentum, which has the largest statistical contribution. In addition, the significance may be improved in Run 3 due to the improved rejection capability of hadron and heavy quark decay muons by MFT.

6 Summary

In this study, we evaluate the detection feasibility of ultra-intense magnetic fields at Runs 2 and 3 with ALICE. A virtual photon polarization measurement, which is one of the QED nonlinear effects, is proposed as a method to detect the ultra-intense magnetic field generated in high energy heavy ion non-central collisions.

First, we theoretically evaluate the virtual photon polarization due to the ultra-intense magnetic field. Since the function of the virtual photon polarization with respect to the Landau level is not obvious, we extrapolated it with several functions. We evaluated systematic uncertainty by extrapolation to infinite sum of Landau levels, and found that the virtual photon polarization is 0.12 ± 0.03 for p_{T}=3.5 GeV/c. Since the higher momentum of virtual photon leads to larger, even larger virtual photon polarization is expected for p_{T}>4 GeV/c.

Next, we estimated the yield of $\gamma^* \to \mu\mu$ and the combinatorial background in Pb-Pb collisions at 5 TeV per nucleon pair by Monte Carlo simulations. The signal in Pb-Pb collisions is estimated by scaling the $\gamma^* \to \mu\mu$ yield from the pp collision simulations to the Run 2 or 3 statistics. We also estimated the yield of combinatorial unlike-sign dimuons in the same event by simulations of Pb-Pb collisions.

Significance was determined based on the above three inputs. As a result, the significance with all dimuons in Run 3 statistics was 0.9σ, and the improvement was expected to be up to 4.3σ by applied p_{T} cut.

We have estimated this without considering the detector effect, but it has the effect of lowering the significance. But, the MFT to be installed at Run 3 will improve hadron and heavy quark decay muons rejection. Therefore, it is worthwhile to perform virtual photon measurements in Run 3.

Acknowledgement

First of all, I would like to express my gratitude to all the people who were involved in the progress of this study. I would like to thank Professor Shigaki-san for his appropriate advice and useful discussions. I could have many opportunities to participate in workshops, and I learned a lot. In particular, oral presentations at international conferences was a very good experience. I would like to thank Associate Professor Ishikawa-san for the theoretical discussions. I am deeply grateful to stuff and students in Quark Physics Laboratory. Associate Professor Yamaguchi-san and Assistant Professor Yano-san gaves me constructive comments and encouragement, and told me the way to use simulations and analysis framework. Ogino-san's support for technical issue of PC were invaluable. Associate Professor Homma-san and Assistant Professor Miyoshi-asn gave me insightful comments in meetings from other fields of study. The advice and encouragement I received from my seniors in the laboratory helped me to think positively about my future career path. Thanks to my colleagues and juniors, I enjoyed my daily life in the laboratory. Finally, I would like to express my gratitude to my family for supporting me in my lab life.

References

[1] H. Koichi and I. Kazunori. Vacuum birefringence in strong magnetic fields:(i) photon polarization tensor with all the landau levels. *Annals of Physics*, 330:23–54, 2013.

[2] K. Hattori and K. Itakura. 強磁場中における真空複屈折の詳細解析とその応用に向けて. http://www2.yukawa.kyoto-u.ac.jp/~soken.editorial/sokendenshi/vol13/netsuba2012/p23-05-Hattori.pdf, 2012.

[3] D. E. Kharzeev, L. D. McLerran, and H. J. Warringa. The effects of topological charge change in heavy ion collisions: " event by event p and cp violation ". *Nuclear Physics A*, 803(3-4):227–253, 2008.

[4] Virtual Journal on QCD Matter. http://qgp.phy.duke.edu.

[5] Paul Stankus. Direct photon production in relativistic heavy-ion collisions. *Annual Review of Nuclear and Particle Science*, 55(1):517–554, 2005.

[6] Jajati K. Nayak. Direct photon productions from Pb+Pb collisions at 2.76 TeV, LHC energy. *DAE Symp. Nucl. Phys.*, 58:730–731, 2013.

[7] A. Tsuji. Evaluations and mesurements of virtual photon polarization dou to intense magnetic field in Pb+Pb collisions at $\sqrt{s_{NN}} = 2.76$ TeV with ALICE, 2014.

[8] K. Hattori. Vacuum birefringence and dichroism in strong magnetic fields. In *The 8th Asian Triangle Heavy-Ion Conference*, 2021.

[9] Fabienne Marcastel. Cern ' s accelerator complex. general photo. https://cds.cern.ch/record/1621583?ln=ja0, 2013.

[10] Martin A. Subieta Vasquez. RESULTADOS DEL EXPERIMENTO ALICE PARA LA FISICA DE RAYOS COSMICOS. *Rev. Bol. Fis.*, 24:7–13, 2014.

[11] Addendum of the Letter of Intent for the upgrade of the ALICE experiment : The Muon Forward Tracker. Technical report, CERN, Geneva, Aug 2013. Final submission of the presetn LoI addendum is scheduled for September 7th.

[12] MFT Collaboration ALICE. ALICE Muon Forward Tracker (MFT). Dec 2020. General Photo.

[13] https://alice-collaboration.web.cern.ch/menu_proj_items/Muon-Spect.

[14] W. Heisenberg and H. Euler. Consequences of dirac theory of the positron, 2006.

[15] RP. Mignani, V. Testa, D. Caniulef, R. Taverna, R. Turolla, S. Zane, and K. Wu. Evidence for vacuum birefringence from the first optical polarimetry measurement of the isolated neutron star rx j1856. 5- 3754. *Monthly Notices of the Royal Astronomical Society*, page stw2798, 2016.

[16] X. Fan, S. Kamioka, T. Inada, T. Yamazaki, T. Namba, S. Asai, J. Omachi, K. Yoshioka, M. Kuwata-Gonokami, A. Matsuo, et al. The oval experiment: a new experiment to measure vacuum magnetic birefringence using high repetition pulsed magnets. *The European Physical Journal D*, 71(11):1–10, 2017.

[17] K. Fukushima, D. E. Kharzeev, and H. J. Warringa. Chiral magnetic effect. *Physical Review D*, 78(7):074033, 2008.

[18] MS. Abdallah, BE. Aboona, J. Adam, L. Adamczyk, J. R. Adams, J. K. Adkins, G. Agakishiev, I. Aggarwal, M. M. Aggarwal, Z. Ahammed, et al. Search for the chiral magnetic effect with isobar collisions at $\sqrt{s_{NN}}$= 200 GeV by the STAR Collaboration at the BNL Relativistic Heavy Ion Collider. *Physical Review C*, 105(1):014901, 2022.

[19] R. Tanizaki. Search for intense magnetic field using deflection of electron-positron pairs in relativistic heavy-ion collisions, 2015.

[20] L. Adamczyk, J. K. Adkins, G. Agakishiev, M. M. Aggarwal, Z. Ahammed, N. N. Ajitanand, I. Alekseev, D. M. Anderson, R. Aoyama, A. Aparin, et al. Global λ hyperon polarization in nuclear collisions. *Nature (London)*, 548(BNL-114181-2017-JA), 2017.

[21] K. I. Ishikawa, D. Kimura, K. Shigaki, and A. Tsuji. A numerical evaluation of vacuum polarization tensor in constant external magnetic fields. *International Journal of Modern Physics A*, 28(20):1350100, 2013.

[22] S L Adler. Photon splitting and photon dispersion in a strong magnetic field. *Annals of Physics*, 67(2):599–647, 1971.

[23] B. Döbrich, H. Gies, N. Neitz, and F. Karbstein. Magnetically amplified light-shining-through-walls via virtual minicharged particles. *Physical Review D*, 87(2):025022, 2013.

[24] F. Karbstein, L. Roessler, B. Döbrich, and H. Gies. Optical probes of the quantum vacuum: the photon polarization tensor in external fields. In *International Journal of Modern Physics: Conference Series*, volume 14, pages 403–415. World Scientific, 2012.

[25] K. Fukushima. Magnetic-field induced screening effect and collective excitations. *Physical Review D*, 83(11):111501, 2011.

[26] K. Kimura. Numerical computation of virtual photon polarization due to ultra-intense magnetic field in the muon detector acceptance at ALICE, 2014.

[27] S. Acharya et al. Υ production and nuclear modification at forward rapidity in Pb-Pb collisions at $\sqrt{s_{NN}}$= 5.02TeV. *Phys. Lett. B*, 822:136579, 2021.

[28] ALICE collaboration et al. Addendum of the letter of intent for the upgrade of the alice experiment: the muon forward tracker. *CERN-LHCC-2013-014*, 2013.

[29] Centrality determination in heavy ion collisions. Aug 2018.